npj | Computational Materials

www.nature.com/npjcompumats

ARTICLE OPEN

Design of 2D massless Dirac fermion systems and quantum spin Hall insulators based on sp–sp^2 carbon sheets

Minwoo Park[1], Youngkuk Kim[2] and Hoonkyung Lee[1]

Grapheneis a massless Dirac fermion system, featuring Dirac points in momentum space. It was also first identified as a quantum spin Hall (QSH) insulator when considering spin–orbit coupling (SOC), which opens a band gap at the Dirac points. This discovery has initiated new research efforts to study the QSH effect, towards its application for quantum computing and spintronics. Although the QSH effect has been observed in HgTe quantum wells, the SOC strength of graphene is too small (~1 μeV) to induce the topological insulator phase in an experimentally achievable temperature regime. Here, we perform a systematic atomistic simulation to design two-dimensional sp–sp^2 hybrid carbon sheets to discover new Dirac systems, hosting the QSH phase. 21 out of 31 newly discovered carbon sheets are identified as Dirac fermion systems without SOC, distinct from graphene in the number, shape, and position of the Dirac cones occurring in the Brillouin zone. Moreover, we find 19 out of the 21 new Dirac fermion systems become QSH insulators with a sizable SOC gap enhanced up to an order of meV, thus allowing for the QSH effect at experimentally accessible temperatures. In addition, based on the 26 Dirac fermion systems, we make a connection between the number of Dirac points without SOC and the resultant QSH phase in the presence of SOC. Our findings present new prospects for the design of topological materials with desired properties.

npj Computational Materials (2018)4:54 ; doi:10.1038/s41524-018-0113-8

INTRODUCTION

Since the first synthesis of graphene,[1] a two-dimensional (2D) atomic layer of sp^2-bonded carbon atoms, it has received tremendous attention due to its unique electronic,[2,3] mechanical, and chemical properties[4–7] as well as unconventional superconducting behavior.[8] The massless Dirac fermions hosted in graphene without spin–orbit coupling (SOC) as quasi-particles allow for fascinating physical phenomena, such as the Klein tunneling and half-integer quantum Hall effects.[2,3] When including SOC, a Dirac fermion system can exhibit even more exciting phenomena related electronic band topology. It was expected that graphene could open a sizable SOC gap at the Dirac point, becoming a 2D topological insulator (TI), supporting quantum spin Hall (QSH) effect. However, the high crystalline symmetries of graphene forbid the first contribution of SOC to the gap opening, reducing the SOC gap down to 10^{-3} meV.[9–11] In order to enhance the SOC, diverse remedies have been explored, including buckling,[12,13] doping,[14] and proximity effect.[15,16] Here, we provide an alternative approach to apply an atomistic design of carbon systems-based sp–sp^2 bonding networks to find diverse carbon-based massless Dirac systems with an enhanced SOC.

Recently, graphyne, a carbon atomic layer structure consisting of acetylene groups (–C≡C–) and sp^2 carbon atoms,[17–20] has been shown to have intriguing electronic properties, such as the coexistence of isotropic and anisotropic Dirac cones in the Brillouin zone (BZ). It has attracted considerable attention due to the shape of the Dirac cones that can give rise to exotic transport and chemical properties. For example, massless Dirac fermions governed by the anisotropic Dirac equation can be used to engineer the electron current with a preferred direction.[21] On the other hand, its porous structure and large surface area may allow for a variety of potential applications in energy storage devices, such as hydrogen storage and lithium-ion batteries as previously studied.[22–24] While these sp^2 carbon systems have been theoretically designed, encouragingly, there has been meaningful progress in experimental efforts for their synthesis.[25–27] For example, graphdiyne, a carbon layer structure consisting of diacetylene groups (–C≡C–C≡C–) and sp^2 carbon atoms, were successfully synthesized in the form of bulk powders,[24] large area films (~4 cm^2),[28,29] and flakes.[30] Carbon ene-yne, a carbon layer structure consisting of diacetylene groups and sp^2 carbon atoms, was also successfully synthesized in a film form.[29] Very recently, ultrathin graphdiyne film on graphene was synthesized using solution-phase van der Waals epitaxy.[31] These experiments have made it more feasible to synthesize sp–sp^2 hybrid carbon sheets as alternating 2D Dirac fermion systems, which can overcome the limitations of graphene.

RESULTS AND DISCUSSION

Design of sp–sp^2 hybrid carbon sheets and Dirac cones

In this paper, we explore new 2D massless Dirac fermion systems, based on a systematic structure search for a variety of 2D sp–sp^2 hybrid networks, comprising sp-bonded carbon chain (–C≡C–)$_n$ and sp^2-bonded carbon atoms. To effectively perform an extensive search for new 2D sp–sp^2 hybrid carbon sheets, we used the following four constraints. (1) sp–sp^2 carbon sheets are built using four building blocks: hexagon, rhombus, triangle, and line shown in Fig. 1a–d. We noticed that this constraint rules out a

[1]Department of Physics, Konkuk University, Seoul 05029, South Korea and [2]Department of Physics, Sungkyunkwan University (SKKU), Suwon 16419, South Korea
Correspondence: Hoonkyung Lee (hkiee3@konkuk.ac.kr)
These authors contributed equally: Minwoo Park, Youngkuk Kim.

Received: 7 May 2018 Revised: 11 September 2018 Accepted: 21 September 2018
Published online: 18 October 2018

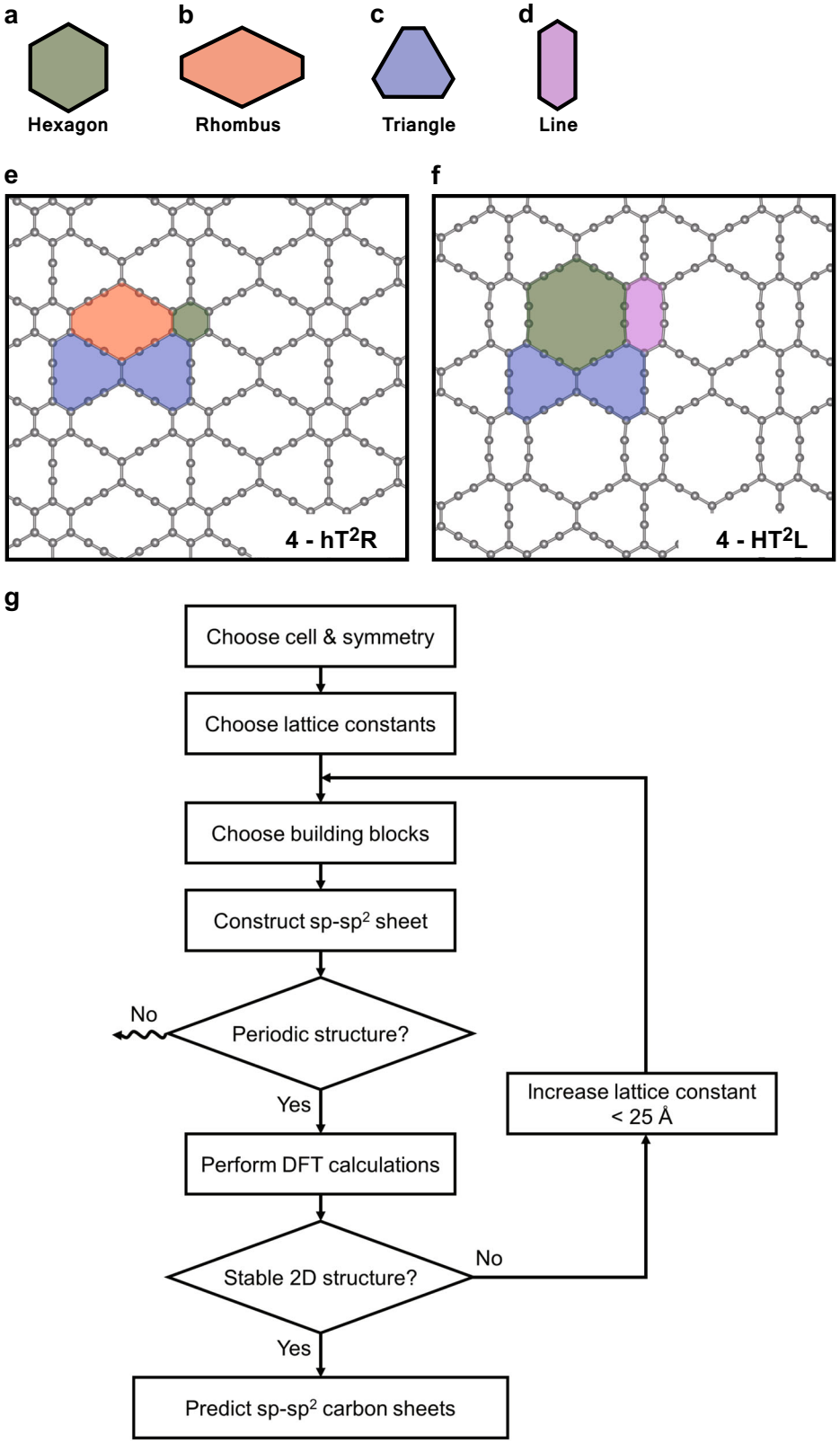

Fig. 1 The design for 2D sp–sp^2 hybrid carbon sheets. Building blocks for designing the layers: **a** hexagon, **b** triangle, **c** rhombus, and **d** line shapes where sp^2-bonded carbon atoms lie on the edge sites of the blocks and zero or even-numbered sp-bonded carbon atoms lie on the line. **e**, **f** show examples for the designed 2D sp–sp^2 hybrid carbon atomic layers. The grey-colored spheres represent carbon atoms and the blocks of a unit cell are colored. **g** Algorithm for predicting 2D sp–sp^2 hybrid carbon sheets based on first-principles calculations

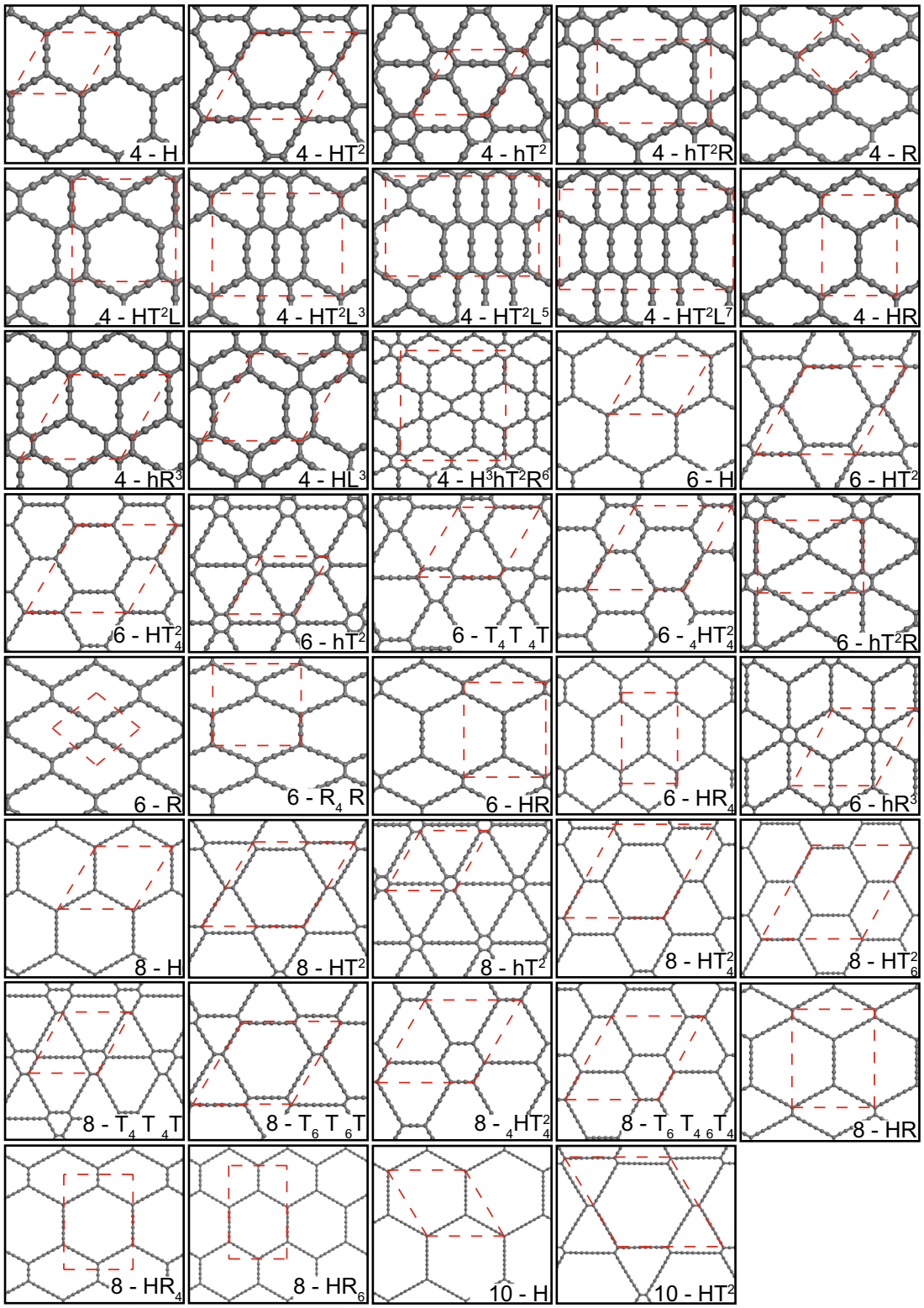

Fig. 2 Atomic structures of designed 2D sp–sp^2 sheets with their notations. Red dotted lines indicate the unit cell

significant number of unrealistic sp–sp^2 hybrid carbon sheets. (2) The bond angles are either 120° or 180°. This constraint ensures carbon atoms to make either sp or sp^2 bond. (3) The bond lengths of triple bond C≡C, double bond C=C, and single bond C–C are set to ~1.24, ~1.38, and ~1.33 Å, respectively, which do not depend on the type of sheets. (4) The lattice constant should be smaller than ~25 Å, which is a reasonable constraint considering that the sheets with larger cell should be rarely synthesized. Based on these constraints, we constructed an algorithm shown in Fig. 1g, which successfully generates the sp–sp^2 carbon sheets presented in Fig. 2. This algorithm also reproduced previous known 2D sp–sp^2 hybrid carbon sheets, such as α-graphyne,

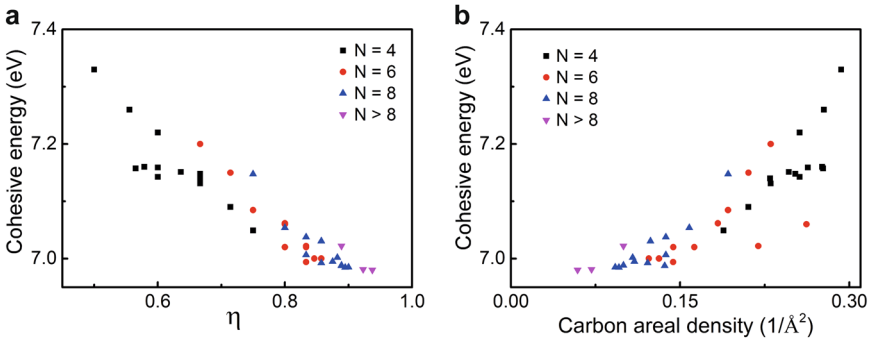

Fig. 3 Cohesive energies of 2D sp–sp^2 hybrid carbon sheets. **a** Cohesive energy as a function of the ratio η between the numbers of sp-bonded carbon atoms (N_{sp}) and sp^2-bonded carbon atoms (N_{sp2}), $\eta = N_{sp}/N_{sp2}$. **b** Cohesive energy as a function of carbon areal density. Colored dots indicate the *N*-geometries, where *N* indicates the number of carbon atoms composing the longest carbon chain. For graphene ($\eta = 0$ and carbon areal density = 0.38/Å), the cohesive energy is calculated to be 7.97 eV

β-graphyne,[17] γ-graphyne,[19] and δ-graphyne.[32] Therefore, we believe that the algorithm that we propose here is highly useful and comprehensive in predicting new sp–sp^2 hybrid carbon sheets.

For instance, some sheets with the four blocks are presented in Fig. 1e, f. The variety of the geometries can be made with a different number of sp-bonded carbon atoms, combinations of the blocks, and symmetries. We use a notation for labeling on the sheets, N–$_l$M^n_k, where *N* denotes the number of carbon atoms of the longest bonds, M denotes H, h, T, R, and L abbreviated for hexagon, hexagon consisting of only sp^2-bonded carbon atoms, triangle, rhombus, and line, respectively. Using a combination of several kinds of block, we follow this order, H, h, T, R, and L, and bigger comes in front for same kinds of M blocks with different *l*, *k*. For given M, the indexes, *l*, *k*, and *n*, respectively denote the number of carbon atoms in the longest bond, the number of carbon atoms in the shortest bond, and the number of same M blocks in a unit cell. To make it simple, there are three omitting rules. First, *l* is omitted when *l* is equal to *N*. Second, *k* is omitted when *k* is equal to 2 or *l*. If and only if $k = l$, it is a hexagon. It does not need *k*. Third, *l* and *k* are omitted when both are equal to 2, substituting h for $_2$H$_2$. For instance, in graphene, which comprises sp^2-bonded carbon atoms and one hexagon in the unit cell, $l = k = 2$, and $n = 1$, thus represented by 2-h. In 6612-graphyne, which is made of one h block, two T blocks with 4 carbon atoms in the longest bond and one R block as shown in Fig. 1e, $N = 4$, $l = k = 2$, $n = 1$ for h, $l = 4$, $k = 2$, $n = 2$ for T, and $l = 4$, $k = 2$, $n = 1$ for R, thus expressed by 4-hT^{2}R. In Fig. 1f, there is one of $N = 4$ family made of one H, two T, and one L blocks, $l = k = 4$, $n = 1$ for H, $l = 4$, $k = 2$, $n = 2$ for T, and $l = 4$, $k = 2$, $n = 1$ for L, thus expressed by 4-HT^{2}L.

We performed systematic design of the sp–sp^2 bonded carbon sheets using our algorithm, resulting in 31 new systems. 2-h is graphene. 4-H, 4-HT^2, 4-hT^2, 4-hT^{2}R, and 4-HT^{2}L are already known as α, β, γ, 6612, and δ-graphyne,[17,19,20,33,34] respectively. 6-H and 6-hT^2 are also known as α and γ-graphdiyne.[35–37] 6-R is reported as carbon ene-yne.[29] The structures with the unit cell and corresponding label are presented in Fig. 2. Here, we only considered a sheet with $N \le 10$ because the cohesive energy significantly decreases as the ratio η between the numbers of sp-bonded carbon atoms (N_{sp}) and sp^2-bonded carbon atoms (N_{sp2}), $\eta = N_{sp}/N_{sp2}$, increases, which is consistent with the previous result[38] in graphyne. In this way, we have found 31 new optimized structures. The calculated cohesive energies as a function of η and areal carbon density are shown in Fig. 3. Among 39 structures, graphyne, which has the structure of 4-hT^2 and is referred to as γ-graphyne, was found to have the largest cohesive energy (7.33 eV) as shown in Table 1, except for graphene, 2-h. This is plausible considering that γ-graphyne has the smallest $\eta = 0.5$. The cohesive energies increase as the carbon areal density increases because the areal density increases as the *N* number increases. The cohesive energy of some of the carbon sheets is close to or even smaller than that of the amorphous carbon (~7.35 eV),[39] which is considered as the thermodynamic limit of synthesis as a free-standing form.[40] Notwithstanding the small cohesive energy, we think that there is much room for 2D materials to avoid the limit as the stability of 2D sheets can be greatly enhanced depending on the substrates. For instance, it was shown that graphdiyne becomes more stable than graphene on the metal surface.[41] Moreover, boron sheets were successfully synthesized on Ag or Au substrates even though they have higher free energy than that of bulk boron. This is again due to the fact that the sheets can be stabilized on the substrates.[42] Similarly, we expect that sp–sp^2 carbon sheets that we predict here should be synthesized on some substrate like a metal surface, overcoming the high free energy in its freestanding form in a vacuum.

Figure 4 shows the calculated band structures for the 39 carbon sheets. 25 out of 39 feature Dirac points in the BZ without SOC, identifying 19 new Dirac fermions systems. 4-H, 4-HT^2, 4-hT^{2}R, 4-hR^3, and 6-H are already reported as Dirac fermions systems.[17,19,34,36,37] While the Dirac points appear in various systems, depending on the system, there are a wide variety of Dirac cones in numbers, shape, and position of Dirac cones in the BZ. Table 1 summarizes the presence and the number of Dirac points with the calculated Fermi velocity. Interestingly, we notice that the occurrence of the archetypical isotropic shape of the Dirac cone that appears in graphene, is rare, only occurring in a few systems such as 6-H and 8-H. The Dirac cone is more isotropic when it occurs at the K point of the BZ in *p6m* space group. The relatively high-symmetric D_{3h} little group of the K point enables the isotropic shape of the Dirac cone in the vicinity of K, although they start to show trigonal warping dispersing away from the K point.[43] For the Dirac cones occurring at a lower-symmetric moment, they appear in an anisotropic shape. More interestingly, in 4-HT^{2}L^3 and 4-hT^{2}R, two anisotropic Dirac cones appear simultaneously along Γ–X and M–X′ high-symmetric lines of the rectangular BZ as shown in Fig. 5a–d. The minimum and maximum Fermi velocities are calculated as 0.40×10^6 and 0.75×10^6 m/s for the Dirac cone in Γ–X, and 0.33×10^6 and 0.63×10^6 m/s for the other Dirac cone in M–X′, respectively. In particular, the maximum anisotropy occurs in 4-H^{3}hT^{2}R^6 in Γ–X (Fig. 5e–g), where the Fermi velocity varies up to 300% as the momentum direction varies. In contrast, 6-R structure has one symmetric Dirac cone (Fig. 5i–l).

We found that isotropic and anisotropic Dirac cones can simultaneously occur in some sp–sp^2 2D systems with the Fermi velocity, largely varying depending on the length of the sp-bonded carbon atoms. More interestingly, the SOC can induce a band gap in the sp–sp^2 2D systems up to an order of meV, which

Table 1. The calculated structural information of the design sp–sp^2 sheets including graphene

Structures	E_c (eV)	Class	l_0 (Å)	v_F (×10^6 m/s)	Symmetry group
2-h	7.97	D	2.46	0.84	*p6m*
4-R	7.15	D	4.91	0.51/0.88	*pmm*
4-hT^{2}R	7.26	D	6.86/9.46	0.46/0.65, 0.30/0.49	*pmm*
4-HT^{2}L	7.15	D	9.34/9.45	0.56/0.63	*pmm*
4-HT^{2}L^3	7.16	D	9.39/ 12.07	0.40/0.75, 0.33/0.63	*pmm*
4-HT^{2}L^5	7.16	D	9.37/ 14.71	0.12/0.64	*pmm*
4-HT^{2}L^7	7.16	S(0.06)	9.37/ 17.34	–	*pmm*
4-HR	7.09	D	7.00/9.50	0.62/0.80	*pmm*
4-H^{3}hT^{2}R^6	7.14	D	16.40/ 18.96	0.11/0.33	*pmm*
4-hR^3	7.22	D	9.50	0.66/0.70	*p6m*
4-HL^3	7.14	D	9.50	0.29/0.68	*p6m*
4-H	7.05	D	7.00	0.70	*p6m*
4-HT^2	7.13	D	9.50	0.29/0.62	*p6m*
4-hT^2	7.33	S(0.47)	6.88	–	*p6m*
6-R	7.06	D	9.50/ 11.50	0.53/0.83	*cmm*
6-R$_4$R	7.02	D	11.00/ 12.00	0.50/0.79	*cmm*
6-hT^{2}R	7.15	D	14.00/9.5	0.41/0.66	*pmm*
6-HR	7.02	D	11.5/14.5	0.57/0.77	*pmm*
6-HR$_4$	7.00	D	11.0/18	0.65/0.69	*pmm*
6-hR^3	7.11	D	14	0.53/0.70	*p6m*
6-H	7.00	D	11.5	0.64	*p6m*
6-HT^2	7.06	S(0.23)	14.5	–	*p6m*
6 − HT$_4^2$	6.99	D	17	0.25/0.62	*p6m*
6-hT^2	7.20	S(0.49)	9.5	–	*p6m*
6-T$_4$T$_4$T	7.08	S(0.09)	12.00	–	*p6m*
6s$_4$HT$_4^2$	7.02	S(0.2)	14.60	–	*p6m*
8-HR	7.00	S(0.39)	16/19.7	–	*pmm*
8-HR$_4$	6.99	D	12.0/22	0.52/0.74	*pmm*
8-HR$_6$	6.98	S(0.34)	16/24.8	–	*pmm*
8-H	6.99	D	15.8	0.58/0.69	*p6m*
8-HT^2	7.03	D	19.8	0.37/0.50	*p6m*
8 − HT$_4^2$	6.99	S(0.19)	22.5	–	*p6m*
8 − HT$_6^2$	6.99	D	25	0.29/0.68	*p6m*
8-hT^2	7.15	S(0.55)	12	–	*p6m*
8-T$_4$T$_4$T	7.05	D	14.8	0.46/0.57	*p6m*
8-T$_6$T$_6$T	7.04	S(0.31)	17.4	–	*p6m*
8-$_4$HT$_4^2$	7.01	S(0.25)	17.4	–	*p6m*
8-T$_6$T$_4^2$$_6T_4$	6.99	S(0.08)	20	–	*p6m*
10-H	6.98	D	20.5	0.56/0.69	*p6m*
10-HT^2	7.02	S(0.28)	25	–	*p6m*

D and S denote Dirac cone and semiconductor with the gap size in eV, respectively
E_c cohesive energy, l_0 lattice constants, v_F Fermi velocity

is significantly enhanced comparing to graphene (~10^{-6} eV), which motivated us to carry out the Z_2 topological invariant calculations, demonstrating experimentally accessible QSH phase hosted in the proposed carbon systems. While many of 2D sp–sp^2 hybrid sheets host massless Dirac fermions in a variety number in the BZ without SOC, most of them become non-trivial Z_2 TIs with sizable band gap opening at the Dirac points. The discovery of diverse Dirac fermion systems without SOC that becomes 2D TI including SOC allows for the generic discussion about the topological origin of the multiple Dirac points based on the crystalline symmetry and the Berry Phase, as well as their connection to the SOC-driven topological phase. Our results should shed light not only on the material realizations of exotic Dirac fermions systems as well as QSH insulators but also on the design principles for the materials with desired properties.

Topological phase and Berry phase of sp–sp^2 carbon sheets

While the shape of Dirac cones is a consequence of the crystalline symmetry, the occurrence of Dirac points is a consequence of the interplay between topology and symmetries. The inversion and time-reversal symmetries quantize the Berry phase without SOC into the Z_2 class[44,45] allowing only either π or 0 values (equivalently $Z_2 = 1$ or 0). The Dirac points carry the nontrivial π Berry phase, which can explain the robust occurrence of the Dirac points in diverse systems. We calculate the Berry phase based on the parity eigenvalues at the four time-reversal invariant momenta (TRIMs),[44,45] which guarantees the presence of an odd number of Dirac points in half the BZ. Consistent with the previous topological discussion,[44,45] our Z_2 invariant calculations result in non-trivial π Berry phase (equivalently, $Z_2 = 1$) for all the systems hosting an odd number of Dirac points in half the BZ (Table 2). Moreover, the systems hosting two Dirac points in half the BZ such as 4-HT^{2}L^3 and 4-hT^{2}R result in trivial 0 Berry phase ($Z_2 = 0$). Therefore, except these two systems, we can conclude that the Dirac points that we find are topologically protected, thus being robust against perturbation preserving inversion and time-reversal symmetries. We also point out that we newly identify a system to host four Dirac points in the BZ and four systems to host six inequivalent Dirac points. These are an exciting discovery to realize exotic multi-Dirac fermion systems, unexpected in known materials.

Similar to graphene,[10] we find that SOC opens a band gap and induces the QSH phase in the Dirac systems of the sp–sp^2 carbon sheets. Unlike graphene, however, the SOC strength, which can be evaluated by half the energy gap opened at Dirac point by SOC,[10] is largely enhanced in many cases of sp–sp^2 carbon sheets. For example, the largest SOC gap is estimated up to ~0.8 meV in the 4-HR case. This value is much greater than the graphene case, which is a few μeV as well as the δ-graphyne case, which is around 0.3 meV.[32] This enhancement of the SOC band gap can be attributed to a relatively low crystalline symmetry of the systems, contrasting to the graphene or δ-graphyne case. In detail, the first order SOC contribution to the band gap is canceled in graphene, due to mirror, allowing only the contribution from the next-nearest p_z hopping symmetries in a view of tight-binding model.[9] In many cases of our systems, such symmetries are absent, thus the first order contribution should survive, explaining the enhanced SOC band gap. We believe the SOC gap is sizable enough to experimentally achieve the QSH phase. In Table 2, we evaluate the SOC gap and the Z_2 topological invariant that characterizes the QSH phase. Out of the 24 Dirac systems, 22 results in nontrivial topological invariant $Z_2 = 1$ hosting the QSH phase.

Interestingly, we have observed that the Z_2 topological invariants that characterized TIs including SOC are equivalent to the Z_2 quantized Berry phase that dictates the existence of the Dirac points without SOC. When a system hosts an odd number of

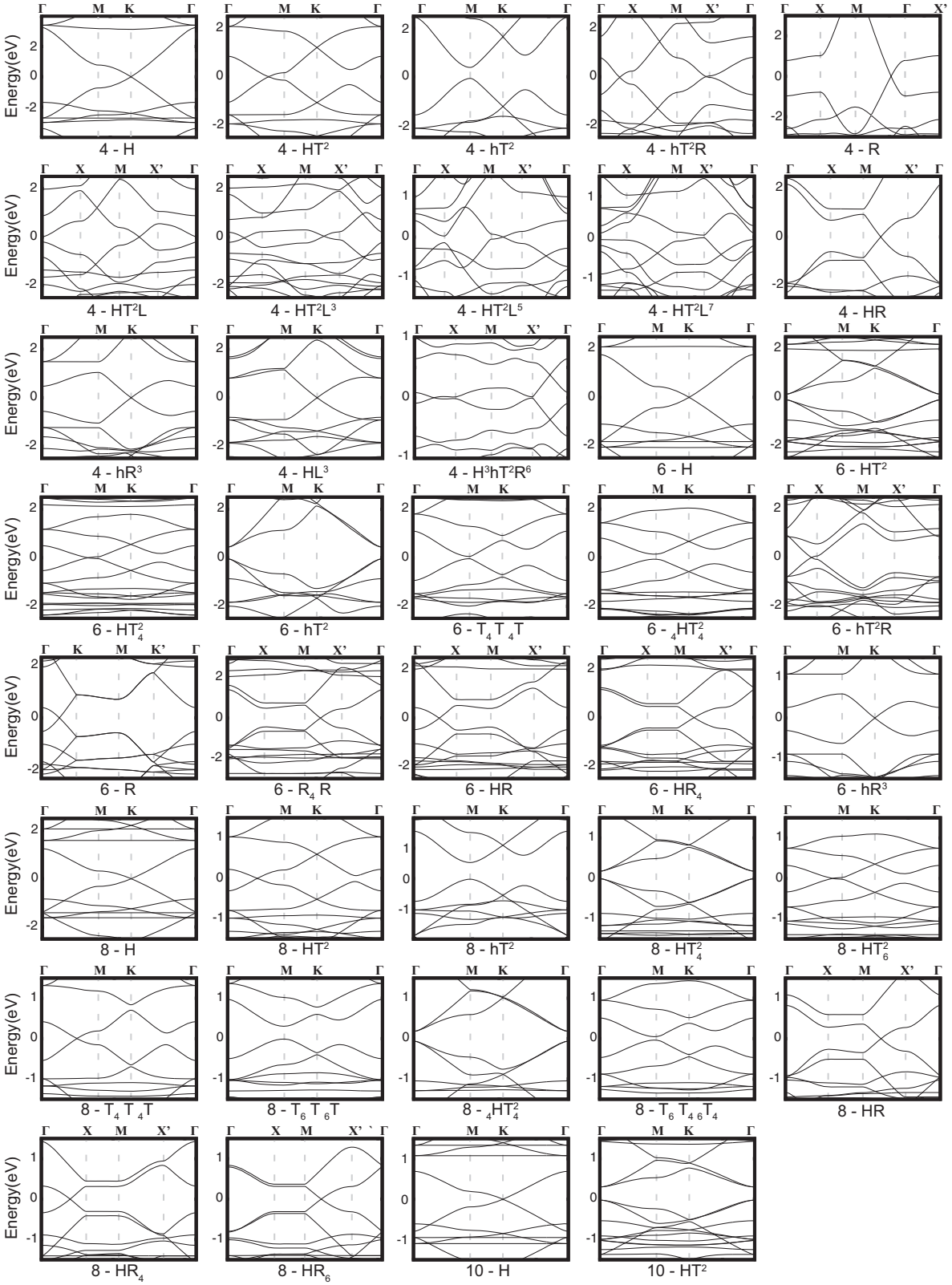

Fig. 4 Energy band structures of the 2D sp–sp^2 sheets. Dirac points at the Fermi level appear in diverse systems. The Fermi level is set to zero

Dirac points in half the BZ without SOC, it is turned out to be that the system carries nontrivial Z_2 topological invariant, indicating the system is a QSH insulator. In the presence of inversion symmetry and without SOC, the non-trivial Z_2 topological Berry phase μ can be evaluated using the parity eigenvalues of occupied bands at four TRIMs in two dimensions $\mu = \prod_{a=1}^{4} \zeta_a$, where

$$\zeta_a = \prod_n \zeta_n(\Gamma_a). \tag{1}$$

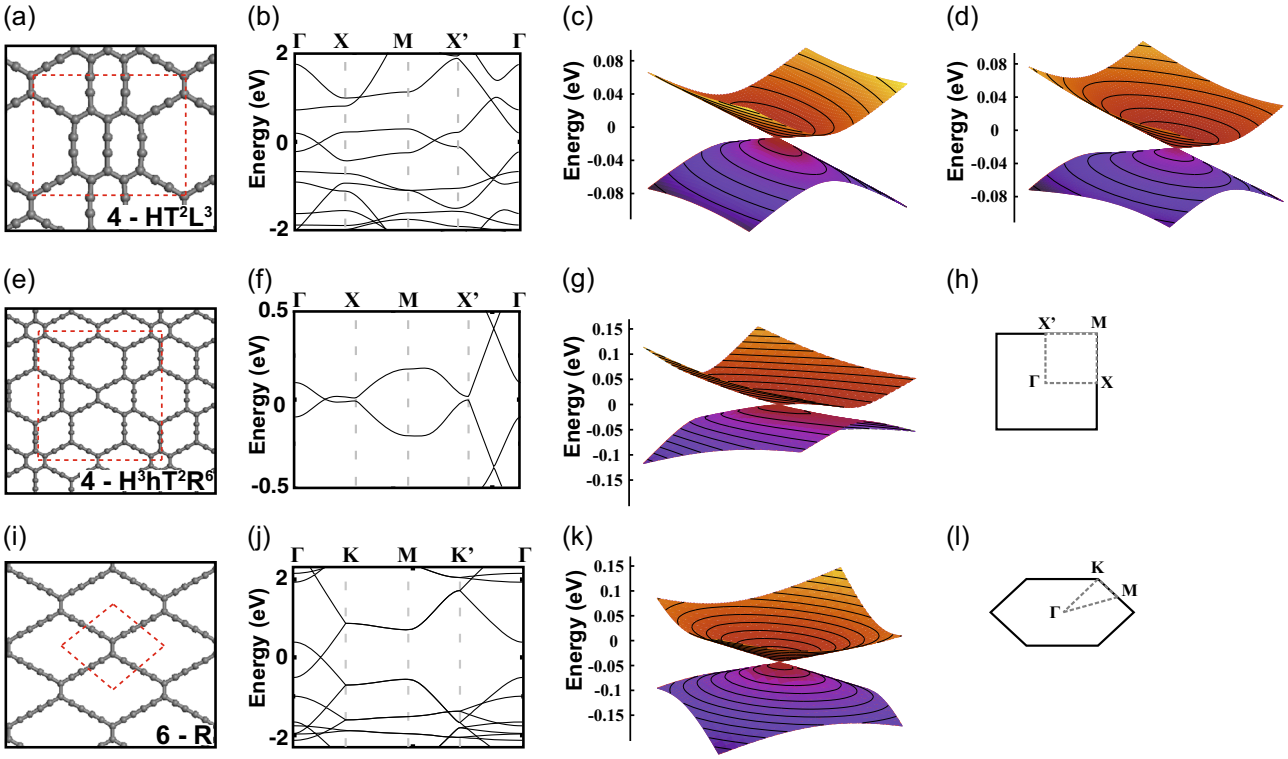

Fig. 5 Atomic structures and the energy bands of specific 2D sp–sp^2 sheets. 4-HT^{2}L^3: **a** atomic structure with a rectangular unit cell, **b** band structure, **c** energy band at Γ–X, and, and **d** energy band at M–X′. 4-H^{3}hT^{2}R^6: **e** atomic structure with a rectangular unit cell, **f** band structure, **g** energy band at Γ–X, and, and **h** BZ for a rectangular unit cell. 6-R: **i** atomic structure with a rhombic unit cell, **j** band structure, **k** energy band at Γ–K, and **l** BZ for a rhombic unit cell. The red dotted lines indicate the unit cells and the Fermi level is set to zero

Table 2. The calculated electronic information of structures with Dirac cones: the number and the location of Dirac cones in half BZ, and value of Z_2

Structures	# of Dirac cones/hBZ	Z_2	Dirac point
2-h	1	1	P(K)
4-R	1	1	L
4-HT^{2}L	1	1	L
4-HT^{2}L^5	1	1	L
4-HR	1	1	L
4-H^{3}hT^{2}R^2	1	1	L
4-hR^3	1	1	P(K)
4-HL^3	1	1	P(K)
4-H	1	1	P(K)
6-R	1	1	L
6-R$_4$R	1	1	L
6-hT^{2}R	1	1	L
6-HR	1	1	L
6-HR$_4$	1	1	L
6-hR^3	1	1	P(K)
6-H	1	1	P(K)
8-HR$_4$	1	1	L
8-H	1	1	P(K)
10-H	1	1	P(K)
4-hT^{2}R	2	0	L
4-HT^{2}L^3	2	0	L
4-HT^2	3	1	L
6−**HT$_4^2$**	3	1	L
8-HT^2	3	1	L
8−**HT$_6^2$**	3	1	L
8-T$_4$T$_4$T	3	1	L

Here, $\zeta_n(\Gamma_a) = \pm 1$ is the parity eigenvalue of the nth occupied energy band at a TRIM point Γ_a. When including SOC, the Dirac points can open a band gap without band inversion at TRIMs becoming either a 2D the time-reversal symmetry-protected TI,[45,46] dictated by the Z_2 topological invariant

$$\zeta_a = \prod_n \zeta_{2n}(\Gamma_a) \quad (2)$$

Here, $\zeta_{2n}(\Gamma_a) = \pm 1$ is the parity eigenvalue of the $2n$th occupied energy band at Γ_a. The $2n-1$th and $2n$th bands are the Kramers pair, which share the same parity eigenvalues, $\zeta_{2n-1} = \zeta_{2n}$. Therefore, Eqs. (1) and (2) result in the same values if SOC preserves the band order at the TRIMs. SOC can preserve the zero gap when the Dirac point occurs at the boundary of the BZ preserved by nonsymmorphic space group symmetries.[46] Therefore, the systems with an odd number of Dirac points in half the BZ can be considered as massless Dirac fermion systems which can be considered as 2D TI in the limit of vanishing SOC. As such, sp–sp^2 carbon networks can be utilized for TIs at a feasible temperature range in experiments.

In conclusion, we have performed a geometry optimization of 2D sp–sp^2 carbon sheets and multilayers of them using the first principles calculations. We found various types of massless Dirac cones systems. The Dirac cones occur in a great diversity in their shape in 2D sp–sp^2 carbon sheets: isotropic or anisotropic Dirac cones, and coexisting asymmetric Dirac cones with different anisotropic directions. Importantly, in sp–sp^2 carbon sheets, the Dirac cones are still remained, but renormalized with respect to graphene. The presence of multiple Dirac points unprecedented in graphene should provide exciting opportunities to encounter novel physics and tailoring the electronic structure and its topological nature. Moreover, the proposed new systems exhibit new possibility to host 2D Z_2 TIs. Our results suggest that Dirac

cone engineering is feasible, which provide frameworks of engineering of Dirac cones and stimulates to search for new TIs.

METHODS

Computational details

Using the density functional theory (DFT), we performed calculations in the Vienna Ab-initio Simulation Package (VASP) with a projector-augmented-wave (PAW) approach.[47] For the exchange-correlation energy functional, the generalized gradient approximation (GGA) was used in the Perdew–Burke–Ernzerhof (PBE) scheme.[48] The kinetic energy cutoff was taken to be 500 eV. Geometrical optimization of our systems was carried out until the Hellmann–Feynman force acting on each atom was smaller than 0.01 eV/Å. The first BZ integration was performed using the Monkhorst–Pack scheme.[49] Corresponded with the size of unit cell, from $4\times4\times1$ to $12\times12\times1$ k-point sampling for the $1\times1\times1$ cell for 2D structures were done. For electronic band structure calculations, from $6\times6\times1$ to $20\times20\times1$ k-point sampling was done. Full-relativistic SOC was considered using the noncollinear formalism based on the all-electron PAW method, as implemented in VASP. For accurate SOC calculations, from $6\times6\times1$ to $30\times30\times1$ k-point sampling was done, which gives converged results.

DATA AVAILABILITY

All data in this work are available from the corresponding author on reasonable request.

ACKNOWLEDGEMENTS

This research was supported by the Basic Science Research Program (NRF-2018R1D1A1B07046751, NRF-2017M3C1B6070572, and NRF-2017R1C1B5018169) through the National Research Foundation of Korea (NRF) funded by the Ministry of Science, ICT & Future Planning. This paper was written as part of Konkuk University's research support program for its faculty on sabbatical leave in 2018. Y.K. acknowledges the support from Institute for Basic Science (IBS-R011-D1).

AUTHOR CONTRIBUTIONS

H.L. conceived and designed the study. M.P. designed new carbon allotropes and nomenclature. M.P. and Y.K. performed the calculations. M.P., Y.K., and H.L. interpreted the data. Y.K., M.P., and H.L. wrote the manuscript. All authors revised the manuscript and approved the final version of the manuscript.

ADDITIONAL INFORMATION

Competing interests: The authors declare no competing interests.

Publisher's note: Springer Nature remains neutral with regard to jurisdictional claims in published maps and institutional affiliations.

REFERENCES

1. Novoselov, K. S. et al. Electric field effect in atomically thin carbon films. *Science* **306**, 666–669 (2004).
2. Zhang, Y., Tan, Y.-W., Stormer, H. L. & Kim, P. Experimental observation of the quantum Hall effect and Berry's phase in graphene. *Nature* **438**, 201–204 (2005).
3. Hirsch, A. The era of carbon allotropes. *Nat. Mater.* **9**, 868–871 (2010).
4. Zhang, D.-B. & Wei, S.-H. Inhomogeneous strain-induced half-metallicity in bent zigzag graphene nanoribbons. *npj Comput. Mater.* **3**, 32 (2017).
5. Papageorgiou, D. G., Kinloch, I. A. & Young, R. J. Mechanical properties of graphene and graphene-based nanocomposites. *Prog. Mater. Sci.* **90**, 75–127 (2017).
6. Hernández Rosas, J. J., Ramírez Gutiérrez, R. E., Escobedo-Morales, A. & Anota, E. C. First principles calculations of the electronic and chemical properties of graphene, graphane, and graphene oxide. *J. Mol. Model.* **17**, 1133–1139 (2010).
7. Qin, G. & Hu, M. Accelerating evaluation of converged lattice thermal conductivity. *npj Comput. Mater.* **4**, 3 (2018).
8. Cao, Y. et al. Unconventional superconductivity in magic-angle graphene superlattices. *Nature* **556**, 43–50 (2018).
9. Konschuh, S., Gmitra, M. & Fabian, J. Tight-binding theory of the spin–orbit coupling in graphene. *Phys. Rev. B* **82**, 245412 (2010).
10. Kane, C. L. & Mele, E. J. Quantum spin Hall effect in graphene. *Phys. Rev. Lett.* **95**, 226801 (2005).
11. van Gelderen, R. & Smith, C. M. Rashba and intrinsic spin–orbit interactions in biased bilayer graphene. *Phys. Rev. B* **81**, 125435 (2010).
12. Luo, W. & Xiang, H. Room temperature quantum spin Hall insulators with a buckled square lattice. *Nano Lett.* **15**, 3230–3235 (2015).
13. Gmitra, M., Kochan, D. & Fabian, J. Spin–orbit coupling in hydrogenated graphene. *Phys. Rev. Lett.* **110**, 246602 (2013).
14. Bonesteel, N. E., Rice, T. M. & Zhang, F. C. Spin–orbit coupling and spirals in doped La_2CuO_4. *Phys. Rev. Lett.* **68**, 2684 (1992).
15. Fu, L. & Kane, C. L. Superconducting proximity effect and majorana fermions at the surface of a topological insulator. *Phys. Rev. Lett.* **100**, 096407 (2008).
16. Stanescu, T. D., Sau, J. D., Lutchyn, R. M. & Sarma, D. S. Proximity effect at the superconductor–topological insulator interface. *Phys. Rev. B* **81**, 241310 (2010).
17. Malko, D., Neiss, C., Viñes, F. & Görling, A. Competition for graphene: graphynes with direction-dependent Dirac cones. *Phys. Rev. Lett.* **108**, 086804 (2012).
18. Coluci, V. R., Braga, S. F., Legoas, S. B., Galvão, D. S. & Baughman, R. H. New families of carbon nanotubes based on graphyne motifs. *Nanotechnology* **15**, S142–S149 (2004).
19. Kim, B. G. & Choi, H. J. Graphyne: hexagonal network of carbon with versatile Dirac cones. *Phys. Rev. B* **86**, 115435 (2012).
20. Narita, N., Nagai, S., Suzuki, S. & Nakao, K. Optimized geometries and electronic structures of graphyne and its family. *Phys. Rev. B* **58**, 11009 (1998).
21. Park, C. H., Son, Y. W., Yang, L., Cohen, M. L. & Louie, S. G. Electron beam supercollimation in graphene superlattices. *Nano Lett.* **8**, 2920–2924 (2008).
22. Hwang, H. J., Kwon, Y. & Lee, H. Thermodynamically stable calcium-decorated graphyne as a hydrogen storage medium. *J. Phys. Chem. C* **116**, 20220–20224 (2012).
23. Hwang, H. J. et al. Multilayer graphynes for lithium ion battery anode. *J. Phys. Chem. C* **117**, 6919 (2013).
24. Zhang, S., Liu, H., Huang, C., Cui, G. & Li, Y. Bulk graphdiyne powder applied for highly efficient lithium storage. *Chem. Commun.* **51**, 1834–1837 (2015).
25. Kehoe, J. M. et al. Carbon networks based on dehydrobenzoannulenes. 3. Synthesis of graphyne substructures. *Org. Lett.* **2**, 969–972 (2000).
26. Yoshimura, T. et al. Synthesis and properties of trefoil-shaped tris(hexadehydrotribenzo[12]annulene) and tris(tetradehydrotribenzo[12]annulene). *Org. Lett.* **8**, 2933–2936 (2006).
27. Johnson, C. A., Lu, Y. & Haley, M. M. Carbon networks based on benzocyclynes. 6. Synthesis of graphyne substructures via directed alkyne metathesis. *Org. Lett.* **9**, 3725–3728 (2007).
28. Li, G. et al. Architecture of graphdiyne nanoscale films. *Chem. Commun.* **46**, 3256–3258 (2010).
29. Jia, Z. et al. Low temperature, atmospheric pressure for synthesis of a new carbon Ene-yne and application in Li storage. *Nano Energy* **33**, 343–349 (2017).
30. Haley, M. M., Brand, S. C. & Pak, J. J. Carbon networks based on dehydrobenzoannulenes: synthesis of graphdiyne substructures. *Angew. Chem. Int. Ed.* **36**, 835 (1997).
31. Gao, X. et al. Ultrathin graphdiyne film on graphene through solution-phase van der Waals epitaxy. *Sci. Adv.* **4**, eaat6378 (2018).
32. Zhao, M., Dong, W. & Wang, A. Two-dimensional carbon topological insulators superior to graphene. *Sci. Rep.* **3**, 3532 (2013).
33. Yang, D. Z., Si, M. S., Zhang, G. P. & Xue, D. S. Crystal momentum-dependent anisotropy of the Dirac cone in the rectangular carbon allotropes. *Europhys. Lett.* **107**, 20003–20007 (2014).
34. Zhang, J., Cui, Y. & Wang, S. Lattice thermal conductivity of δ-graphyne—a molecular dynamics study. *Phys. E: Low-Dimens. Syst. Nanostruct.* **90**, 116–122 (2017).
35. Jang, B. et al. Graphdiyne as a high-capacity lithium ion battery anode material. *Appl. Phys. Lett.* **103**, 263904 (2013).
36. Li, Y., Xu, L., Liu, H. & Li, Y. Graphdiyne and graphyne: from theoretical predictions to practical construction. *Chem. Soc. Rev.* **43**, 2572 (2014).
37. Niu, X. et al. Dirac cone in α-graphdiyne: a first-principles study. *Nanoscale Res. Lett.* **8**, 469 (2013).
38. Shin, H. et al. Cohesion energetics of carbon allotropes: quantum Monte Carlo study. *J. Chem. Phys.* **140**, 114702–114707 (2014).
39. Tersoff, J. Empirical interatomic potential for carbon, with applications to amorphous carbon. *Phys. Rev. Lett.* **61**, 2879–2882 (1988).
40. Aykol, M., Dwaraknath, S. S., Sun, W. & Persson, K. A. Thermodynamic limit for synthesis of metastable inorganic materials. *Sci. Adv.* **4**, eaaq0148 (2018).
41. Han, N., Liu, H., Zhou, S. & Zhao, J. Possible formation of graphyne on transition metal surfaces: a competition with graphene from the chemical potential point of view. *J. Phys. Chem. C* **120**, 14699–14705 (2016).
42. Mannix, A. J., Zhang, Z., Guisinger, N. P., Yakobson, B. I. & Hersam, M. C. Borophene as a prototype for synthetic 2D materials development. *Nat. Nanotechnol.* **13**, 444 (2018).

43. Herbut, I. F. Explanation for the isotropy of the Dirac cone in graphene. *Phys. Rev. B* **79**, 193405 (2009).
44. Kariyado, T. & Hatsugai, Y. Symmetry-protected quantization and bulk-edge correspondence of massless Dirac fermions: application to the fermionic Shastry–Sutherland model. *Phys. Rev. B* **88**, 245126 (2013).
45. Kim, Y., Wieder, B. J., Kane, C. L. & Rappe, A. M. Dirac line nodes in inversion-symmetric crystals. *Phys. Rev. Lett.* **115**, 036806 (2015).
46. Wieder, B. J., Kim, Y., Rappe, A. M. & Kane, C. L. Double Dirac semimetals in three dimensions. *Phys. Rev. Lett.* **116**, 186402 (2016).
47. Kresse, G. & Joubert, D. From ultrasoft pseudopotentials to the projector augmented-wave method. *Phys. Rev. B* **59**, 1758–1775 (1999).
48. Perdew, J. P., Burke, K. & Ernzerhof, M. Generalized gradient approximation made simple. *Phys. Rev. Lett.* **77**, 3865–3868 (1996).
49. Monkhorst, H. J. & Pack, J. D. Special points for Brillouin-zone integrations. *Phys. Rev. B* **13**, 5188–5192 (1976).